The Astrophysical Journal Letters, 962:L6 (7pp), 2024 February 10 https://doi.org/10.3847/2041-8213/ad1de1

Rapid Chemical Enrichment by Intermittent Star Formation in GN-z11

Chiaki Kobayashi[1] and Andrea Ferrara[2]
[1] Centre for Astrophysics Research, Department of Physics, Astronomy and Mathematics, University of Hertfordshire, Hatfield, AL10 9AB, UK
c.kobayashi@herts.ac.uk
[2] Scuola Normale Superiore, Piazza dei Cavalieri 7, 56126 Pisa, Italy
Received 2023 August 29; revised 2023 December 22; accepted 2024 January 12; published 2024 February 6

Abstract

We interpret the peculiar supersolar nitrogen abundance recently reported by the James Webb Space Telescope observations for GN-z11 ($z = 10.6$) using our state-of-the-art chemical evolution models. The observed CNO ratios can be successfully reproduced—independently of the adopted initial mass function, nucleosynthesis yields, and presence of supermassive ($>1000M_{\odot}$) stars—if the galaxy has undergone an intermittent star formation history with a quiescent phase lasting ∼100 Myr, separating two strong starbursts. Immediately after the second burst, Wolf–Rayet stars (up to $120M_{\odot}$) become the dominant enrichment source, also temporarily (<1 Myr) enhancing particular elements (N, F, Na, and Al) and isotopes (^{13}C and ^{18}O). Alternative explanations involving (i) single burst models, also including very massive stars and/or pair-instability supernovae, or (ii) pre-enrichment scenarios fail to match the data. Feedback-regulated, intermittent star formation might be common in early systems. Elemental abundances can be used to test this hypothesis and to get new insights on nuclear and stellar astrophysics.

Unified Astronomy Thesaurus concepts: Chemical abundances (224); Galaxy formation (595); Galaxy evolution (594); Stellar nucleosynthesis (1616); Interstellar abundances (832); Galaxy abundances (574); Wolf-Rayet stars (1806); Population III stars (1285)

1. Introduction

The James Webb Space Telescope (JWST) is expected to find the first galaxies—those that host or have hosted metal-free (known as Population III) stars. Surprisingly, though, one of the most distant galaxies detected, GN-z11 at redshift $z = 10.6$, showed strong metal lines (Bunker et al. 2023). Even more puzzlingly, GN-z11 shows an unusually high (>4× solar) N/O ratio. Supermassive stars have been suggested (e.g., Charbonnel et al. 2023; Nagele & Umeda 2023; Senchyna et al. 2023) as the N source in GN-z11. Is such an unusual stellar population truly required, or would it be possible to reproduce the observations more simply with a varying star formation history?

At the end of the "dark ages" of the Universe, the cosmic dawn was heralded by the birth of the first stars and galaxies. The first cosmic star formation is driven by inefficient cooling from hydrogen molecules. Thus, on general grounds, the first stars were expected to be massive, with masses $M_{\star} \approx 100M_{\odot}$ (e.g., Abel et al. 2002; Bromm & Larson 2004). However, the initial stellar mass depends on complex physical processes, such as gas fragmentation, ionization, accretion, and feedback from newborn stars. Once these processes are included in modern numerical simulations, it seems possible to form lower-mass stars (Greif et al. 2011; Hirano et al. 2014; Rossi et al. 2021), and even binaries (Stacy & Bromm 2013; see also Hartwig et al. 2023 for observational signatures).

The properties of the first stars, i.e., mass, rotation, multiplicity, and magnetic fields, are important for the reionization and chemical enrichment of intergalactic medium, seeding of supermassive black holes (BHs), and gravitational wave emission. However, a direct detection of Population III stars is still lacking, i.e., no zero-metal star or galaxy has yet been found. Instead, the nature of the first stars has been studied using the second generation of stars born out of gas enriched by Population III stars.

There is a consensus that second-generation stars can be found among extremely metal-poor (EMP; [Fe/H] < −3) stars in the Milky Way (Beers & Christlieb 2005) and in dwarf spheroidals (Skúladóttir et al. 2021). From the analysis of the elemental abundances of EMP stars, it has been deduced that the first enrichment sources were likely to be $M_{\star} \approx 10$–$40M_{\odot}$ stars, which exploded as "faint" supernovae (e.g., Umeda & Nomoto 2003; Ishigaki et al. 2018). Similar results are obtained also for quasar absorption line systems, such as metal-poor damped Lyα systems (DLAs), where accurate (barring uncertainties on dust depletion) elemental abundances are measured (Kobayashi et al. 2011; Saccardi et al. 2023).

Theoretically, stellar rotation becomes more important at low metallicities, because weaker stellar winds result in a smaller angular momentum loss than at solar metallicity. As a result, if massive stars are fast rotators, rotational mixing brings CNO cycle products into the convective He-burning layers, and the stellar envelope containing light elements such as C, N, and F may be ejected in stellar winds of Wolf–Rayet (WR) stars (Meynet & Maeder 2002; Limongi & Chieffi 2018); without them, the N abundance is a dex lower (see Figure 9 of Kobayashi & Taylor 2023). WR stars can also explain the detection of highly enhanced hydrogen fluoride in NGP190387 at $z = 4.42$, a dusty star-forming galaxy discovered by the Atacama Large Millimeter/submillimeter Array (ALMA; Franco et al. 2021).

In addition to NGP190387, and rather unexpectedly, many high-redshift galaxies contain large ($\simeq 10^7 M_{\odot}$) amounts of dust (e.g., Ferrara et al. 2022; Inami et al. 2022). Although supernovae are usually considered the main sources at high-z

Table 1
Input Parameters Describing the Adopted Star Formation Histories Shown in Figures 2 and 4

	t_1 (Gyr)	t_2 (Gyr)	$\tau_{i,1}=\tau_{i,2}$ (Gyr)	$\tau_{s,1}$ (Gyr)	$\tau_{s,2}$ (Gyr)	$f_{g,0}$	t_{age}^{max} (Myr)	$\langle t_{age}\rangle_M$ (Myr)	ψ (Gyr^{-1})	log O/H +12	log N/O
Single starburst	⋯	⋯	0.001	0.0002	⋯	0	4.2	3	22	7.787	−2.198
Dual starburst (fiducial)	0.1	0.2	0.001	0.2	0.0002	0	204	26	20	7.850	0.246
Dual starburst	0.05	0.1	0.001	0.2	0.0002	0	103	9	28	7.754	−0.033
Dual starburst	0.1	0.1	0.001	0.2	0.0002	0	103	11	38	7.754	0.047
Dual starburst	0.1	0.2	0.01	0.2	0.0002	0	204	34	41	7.769	0.208
Dual starburst	0.1	0.2	0.001	0.2	0.001	0	205	27	33	7.864	−0.081
Pre-enrichment	⋯	⋯	0.001	0.0002	⋯	0.3	2.8	2	58	7.768	−0.374
GN-z11	...	...	...	...	...	...	19^{+10}_{-5}	10^{+3}_{-2}	19^{+23}_{-12}	7.82	> -0.25

Note. Here, t_1 and t_2 are the beginning (end) of the first burst in dual burst models. The formation epoch t_{age}^{max} is chosen to match the observed O/H. The last four columns are model output values at the observed epoch ($z = 10.6$): mass-weighted age of stars $\langle t_{age}\rangle_M$, star formation rate ψ, mass-weighted O abundance, and N/O ratio. The observed values are taken from Bunker et al. (2023).

($z \sim 7$; Todini & Ferrara 2001; Dayal et al. 2022; Witstok et al. 2023), dust can be produced also by WR stars (e.g., Lau et al. 2022).

The earliest JWST observations have revealed an unexpected abundance of super-early ($z > 10$), massive ($M_* \approx 10^9 M_\odot$) galaxies at the bright end ($M_{UV} \approx -21$) of the ultraviolet luminosity function. These galaxies tend to have very blue spectral slopes ($\beta < -2.4$). Hence, the dust produced by massive stars associated with the observed stellar population must have been efficiently evacuated (or destroyed) along with most of the gas by powerful galactic outflows driven by the radiation pressure produced by their compact ($\simeq$100 pc), young (20–30 Myr) stellar component (Ferrara et al. 2023; Fiore et al. 2023; Ziparo et al. 2023). Such feedback temporarily quenches star formation (Gelli et al. 2023; Looser et al. 2023) until the gas content of the galaxy is restored by efficient cosmological gas accretion, entailing a duty cycle of $\simeq$50–100 Myr.

In this Letter, we aim to construct a scenario connecting these observations with galactic chemical evolution (GCE) models. As different chemical elements are produced by stars with different masses on different timescales, their abundance ratios can uniquely constrain the star formation and enrichment histories of galaxies.

2. Models

2.1. Galactic Chemical Evolution Models

We use the GCE code from Kobayashi et al. (2000), implementing the so-called one-zone model, which integrates the following equation:

$$\frac{d(Z_i f_g)}{dt} = E_{SW} + E_{SNcc} + E_{SNIa} - Z_i\psi + Z_{i,inflow}R_{inflow} - Z_i R_{outflow}, \quad (1)$$

where the mass fraction Z_i of each element i in gas-phase (f_g denotes the gas fraction[3]) increases via element production (E_{SW}, E_{SNcc}, and E_{SNIa}); the other terms are star formation ($\psi = f_g/\tau_s$), gas inflow $R_{inflow} = \exp(-t/\tau_i)/\tau_i$, and outflow ($R_{outflow}$) rates, respectively. The model assumes instantaneous mixing of the elements but not instantaneous recycling. A complete description can be found in Kobayashi et al. (2000) and Kobayashi & Taylor (2023, hereafter KT23). The adopted parameters are summarized in Table 1.

The code includes the latest nucleosynthesis yields of asymptotic giant branch (AGB) stars, super-AGB stars, and core-collapse supernovae (including hypernovae and failed supernovae) from Kobayashi et al. (2020a, hereafter K20), as well as WR stars described in Section 4.1. Type Ia supernovae are also included (E_{SNIa}) using the model in Kobayashi & Nomoto (2009) and yields from Kobayashi et al. (2020b). However, their contribution becomes important only at [Fe/H] $\gtrsim -1$.

The compositions of the infalling gas ($Z_{i,inflow}$) is set to be primordial (see Section 2.2.1 of K20). All models presented in this Letter have no stars at the start. Our fiducial model assumes initial gas fraction $f_{g,0} = 0$, but we also present a pre-enriched model with $f_{g,0} = 0.3$ and initial composition ($Z_{i,0}$) deduced from another GCE model.

The initial mass function (IMF), taken from Kroupa (2008), is a broken power law in three mass ranges. Later in Section 4, we vary the massive-end slope x, and lower and upper mass limits [m_ℓ, m_u] for the Population I/II and III stars, separately. These two IMFs are switched at the threshold (absolute) metallicity $Z_{th} = 0.0001$.

It is important to note that our adopted nucleosynthesis yields reproduce the observed elemental abundances in the Milky Way with the standard IMF: $x = 1.3$, $m_\ell = 0.01 M_\odot$, and $m_u = 120 M_\odot$. This is fundamentally different from the recent modeling works by Bekki & Tsujimoto (2023), Isobe et al. (2023), and Marques-Chaves et al. (2024).

3. Results

3.1. Single Burst Models

We first assume a single starburst starting 4 Myr before the observed epoch; this is because the estimated age of GN-z11 stellar populations is $\sim$10 Myr (Bunker et al. 2023). The corresponding star formation rate per unit mass is shown as a green short dashed line in Figure 1.

The left panels of Figure 2 show the elemental abundance ratios of the interstellar medium (ISM) predicted by the GCE models as a function of time, while the middle panels logO/H +12, a commonly used proxy for metallicity.[4]

[3] Ratio of gas mass to the total mass provided by gas, stars in the galaxy, and the gas "reservoir", i.e., $\int_0^\infty R_{inflow}\, dt + f_{g,0} = 1$, where $f_{g,0}$ is the initial gas fraction.

[4] The solar oxygen abundance adopted in K20 is 8.76.

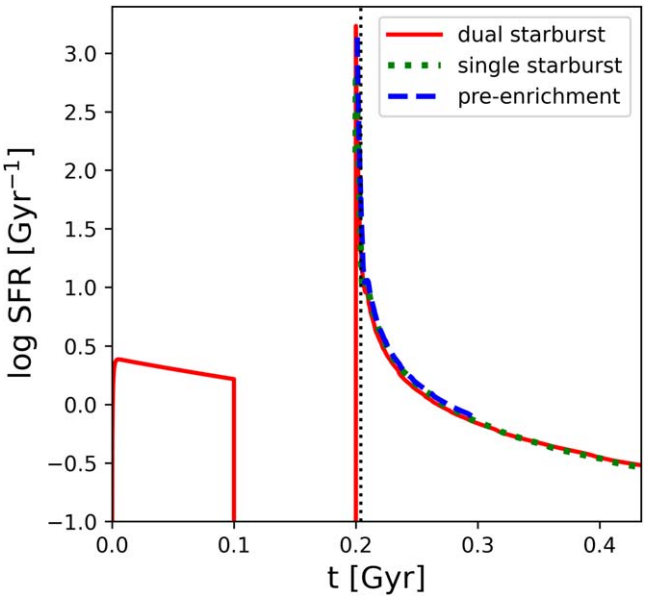

Figure 1. Star formation history adopted by three different GCE models for GN-z11: single starburst (green short dashed line); dual starburst (red solid); and single burst with pre-enrichment (blue long dashed). The vertical dotted line denotes the observed epoch of GN-z11.

At low metallicities, WR stars produce very high (C,N)/O ratios, which quickly decrease due to the large O production from supernovae. The N/O ratio increases again at high metallicities because of "primary" production of N from AGB stars, as well as "secondary" production of N (from initially existing CNO) in massive stars. For the same reason, the initial C/N ratio increase is followed by a rapid drop at high metallicities.

In general, a shorter τ_s shifts the CNO tracks to the right in the middle panels. However, the adopted τ_i and τ_s values (Table 1) are very short, compared with those for present-day massive galaxies. Even shorter τ_s values do not affect the solution any further. The CNO tracks are insensitive to τ_i. In conclusion, although N/O can be high at very low or very high metallicities, with a single starburst it is not possible to reproduce the observed ratio of GN-z11 at the observed oxygen abundance (7.82; Cameron et al. 2023).

3.2. Dual Burst Models

We have seen that WR stars can potentially produce high (C,N)/O ratios, but only at metallicities much lower than observed. However, there is a way to overcome the problem, and this consists of assuming a dual starburst model. We now assume that star formation starts[5] at $z \sim 16.7$ and continues for 100 Myr (Figure 1); the infall and star formation timescales are set to $\tau_i = 0.001$ and $\tau_{s,1} = 0.2$ Gyr, respectively.[6]

The results of this fiducial model (red curve) are shown in the left and middle panels of Figure 2. After the first burst the metallicity already reaches log O/H +12 = 8.5, and the evolutionary tracks up to this point are similar to those for the single burst case.

Then, star formation is assumed to be completely quenched for 100 Myr,[7] possibly due to feedback associated with the onset of an outflow. At $t = 0.2$ Gyr, the secondary infall ($\tau_i = 0.001$ Gyr) of primordial gas occurs, which initially causes dilution reducing the metallicity. As a more extreme second starburst ($\tau_{s,2} = 0.2$ Myr)[8] is triggered, WR stars quickly enhance (C,N)/O ratios until supernovae produce a large amount of O. The O abundance peaks at $t = 0.207$ Gyr, which corresponds to the lifetime of $\sim 30 M_\odot$ stars, and gradually decreases until $t = 0.23$ Gyr. This, along with secondary N production from metal-rich SNe and primary N production from AGB stars (lifetime ∼40–150 Myr), leads to a final N/O increase.

This N/O evolution predicted by the dual burst fiducial model crosses the observed range only once, at $t = 0.204$ Gyr, i.e., 4 Myr after the onset of the second burst (the right panels of Figure 2). The time spent in the data box is very short (∼0.6 Myr). Hence, we conclude that N-enriched objects similar to GN-z11 might be rare. On the other hand, lower ratios than in GN-z11 (e.g., log N/O = −0.4 at $z \sim 6$ in Isobe et al. 2023) can be reproduced in our scenario with longer $\tau_{s,2}$. In this case, the evolution is slower and these objects become more common.

At the observed epoch, the star formation rate in the fiducial model is 20 Gyr^{-1}. This is in excellent agreement with the observed value $\sim 19 M_\odot$ yr^{-1}, provided the total stellar mass is $M_\star \sim 10^9 M_\odot$. The amount of stars formed during the first burst is only 16% of the final stellar mass. The mass-weighted age is 26 Myr, which is comparable to the estimated value of ∼10 Myr. With shorter first bursts and/or shorter quiescence intervals, the mass-weighted age could be made as short as ∼10 Myr.

3.3. Pre-enrichment?

An alternative way to change the gas metallicity before the first starburst is by pre-enrichment from external galaxies. This model is shown in Figure 2, the left and middle panels (blue long dashed curve), where it is also compared with the single and dual burst cases.

The pre-enriched model assumes the same τ_i and τ_s as in the single burst one (Table 1), but with a gas chemical composition, $Z_{i,0}$, taken from another (independent) GCE model with $\tau_{i,0} = 1$ and $\tau_{s,0} = 0.3$ Gyr. We set the initial gas fraction $f_{g,0} = 0.3$. These $f_{g,0}$ and $Z_{i,0}$ values are very similar to those obtained for the dual starburst model during the interval after the first burst, i.e., at $t = 0.1$–0.2 Gyr. However, in this case, the initial stellar fraction is zero, which is the key difference from the dual burst model (red curve).

The pre-enrichment model starts at log O/H +12 = 8.3. Due to the dilution with the infalling pristine gas, the metallicity (horizontally) decreases keeping the same CNO ratios. The (C, N)/O ratios quickly (vertically) increase due to enrichment from WR stars, and they return to their initial composition values. Hence, the triangle track does not cross the observed range. The above results are insensitive to the parameters of τ_i and τ_s. By changing the initial gas fraction $f_{g,0}$ and/or the initial composition $Z_{i,0}$, we cannot find any tracks that match the

[5] Results are insensitive to the formation epoch, and thus pre-enrichment from Population III stars formed at $z \gtrsim 20$ is included in this subsection.

[6] The allowed range is $\tau_{s,1} = 0.1$–1 Gyr, so that the ISM is sufficiently enriched by the initial star formation. Results are insensitive to τ_i.

[7] A marginally consistent, lower-quality fit can nevertheless be obtained also without a quiescent interval between the two bursts.

[8] The condition to reach the observed N/O is $\tau_{s,2} \leqslant 1$ Myr.

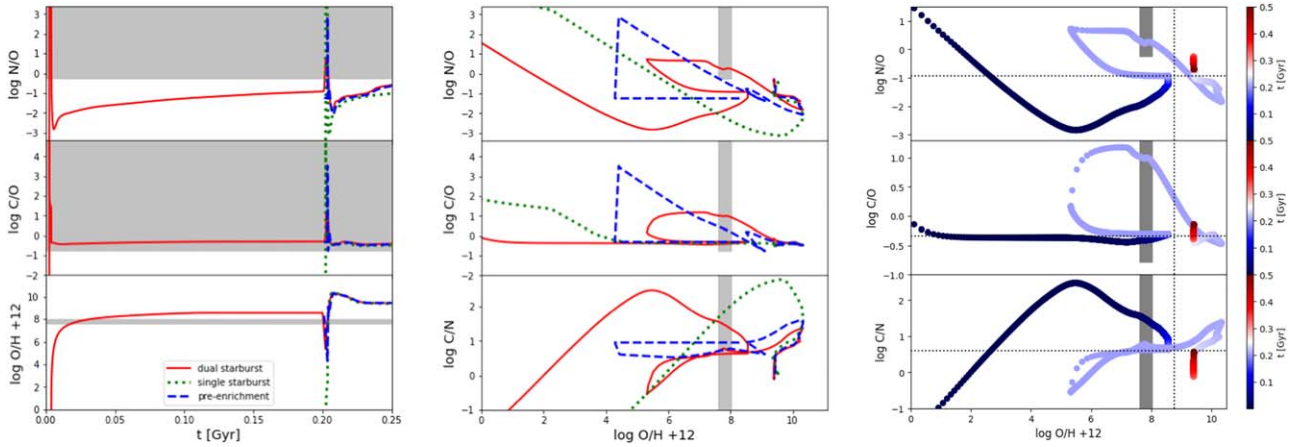

Figure 2. Evolution of CNO abundance ratios (by number), compared to the observational data for GN-z11 (Cameron et al. 2023; gray areas/bars). Left panels: as a function of time, for the same models in Figure 1 including WR stars and standard IMF. Middle panels: similar to the left panels but as a function of gas oxygen abundance. Right panels: same as the middle panels but only for our fiducial model, i.e., dual starburst with standard IMF, color-coded with the time (in Gyr) elapsed since the first star formation episode. The dotted lines indicate the solar ratios.

observed abundance range. We conclude that this simple pre-enrichment prescription cannot solve the problem at hand.

4. IMF Dependence

4.1. Fate of Massive Stars

While the ultimate fate of stars depends on their initial mass,[9] the final mass and nucleosynthesis yields are determined by stellar mass-loss (e.g., Vink et al. 2011) as well as convection treatment and nuclear reaction rates. We include nucleosynthesis yields covering a full mass range up to $1000M_\odot$ as follows.

10–$50M_\odot$: These stars become core-collapse supernovae. Although Limongi & Chieffi (2018) provided yields including explosive nucleosynthesis, their yields do not match observations in the Milky Way, probably because of the lack of hypernovae and mixing fallback. Therefore, we combine their stellar wind yields (see below) with the explosive nucleosynthesis yields of CO cores from K20, which result in an excellent agreement with the observations of almost all elements.[10] Roughly half of stars with 20–$50M_\odot$ are assumed to explode as hypernovae leaving a BH, probably due to rotation and/or binary interaction. The exact fraction of hypernovae can be determined from chemodynamical simulations of a Milky Way-type galaxy; Kobayashi & Nakasato (2011) find $\epsilon_{\rm HN} = (0.5, 0.5, 0.4, 0.01, 0.01)$ for $Z = (0, 0.001, 0.004, 0.02, 0.05)$. All stars with 13–$20M_\odot$, and the rest of stars with 20–$30M_\odot$, explode as normal core-collapse supernovae with 10^{51} erg of explosion energy, leaving a neutron star. The rest of stars with 30–$50M_\odot$ are assumed to be "failed" supernovae, which form a $\sim 10M_\odot$ BH. This is based on the unsuccessful explosion simulations of such massive stars (Janka 2012; Burrows & Vartanyan 2021) and the lack of massive progenitors expected at supernova locations in HST data (Smartt 2009), but the threshold was determined from GCE models (Figure 4 of K20).

60–$140M_\odot$: Stars above $\sim 90M_\odot$ become *pulsating pair-instability supernovae*. Their evolution and nucleosynthesis are uncertain, but they will leave a $\sim 100M_\odot$ BH. Although this phase is not calculated, we use the stellar wind yields from Limongi & Chieffi (2018) for 13–$120M_\odot$ with four different metallicities and three rotational velocities. With rotation, lower-mass stars become WR stars. We apply rotating models to a metallicity-dependent fraction $\epsilon_{\rm HN}(Z)$ (given above) of the stars; among these, 3% (97%) rotate at 300 (150) km s^{-1}. The remaining $1 - \epsilon_{\rm HN}(Z)$ fraction of stars are assumed to be nonrotating.

160–$280M_\odot$: If the masses of the first stars are $\sim$160–$280M_\odot$, they explode as pair-instability supernovae (PISNe; Barkat et al. 1967; Heger & Woosley 2002; Nomoto et al. 2013; Takahashi et al. 2018) leaving no remnant. PISNe have a very distinct nucleosynthetic pattern. Although considerable effort has been made to detect such a characteristic pattern, no observational signature for the existence of PISNe has yet been convincingly found, neither in EMP stars (Cayrel et al. 2004; Aguado et al. 2023) nor in DLAs (Kobayashi et al. 2011; Saccardi et al. 2023). We apply a mix of nonmagnetic, rotating, and nonrotating models from Takahashi et al. (2018) at $Z = 0$ only, using $\epsilon_{\rm HN}(Z)$ described above.

300–$1000M_\odot$: Very-massive stars (VMSs; $>100M_\odot$) have been solidly identified in the Tarantula Nebula of the Large Magellanic Cloud (Schneider et al. 2018). Various stellar evolution models (e.g., Szécsi et al. 2022), and some nucleosynthesis yields (Yusof et al. 2013; Martinet et al. 2022; Volpato et al. 2023) exist, although the results significantly depend on the input physics. We take the nucleosynthesis yields of the "max" mass-loss models from Volpato et al. (2023) for 300–$1000M_\odot$ and 100–$1000M_\odot$ at metallicity $Z = 0$ and 0.0002, respectively. We also take the stellar wind yields of the V11 models from Higgins et al. (2023) for 100–$500M_\odot$ at $Z = 0.014$, assuming very strong winds from Vink et al. (2011). N production is seen as a result of the CNO cycle during core H-burning. These yields do not include explosive nucleosynthesis (i.e., stellar winds only).

We do not include supermassive stars (SMSs; $>1000M_\odot$) in our GCE models, as their properties and yields are uncertain. SMSs are originally defined as those that collapse on the

[9] With the term *initial mass* we refer to single stars, as stars can lose their envelope also due to binary interactions.

[10] At $Z = 0$, some stars in the range 13–$40M_\odot$ may explode as "faint" supernovae/hypernovae. These stars produce only a tiny amount of iron because of the relatively large remnant BH ($\sim 5M_\odot$). Their contribution is negligible and is not included here.

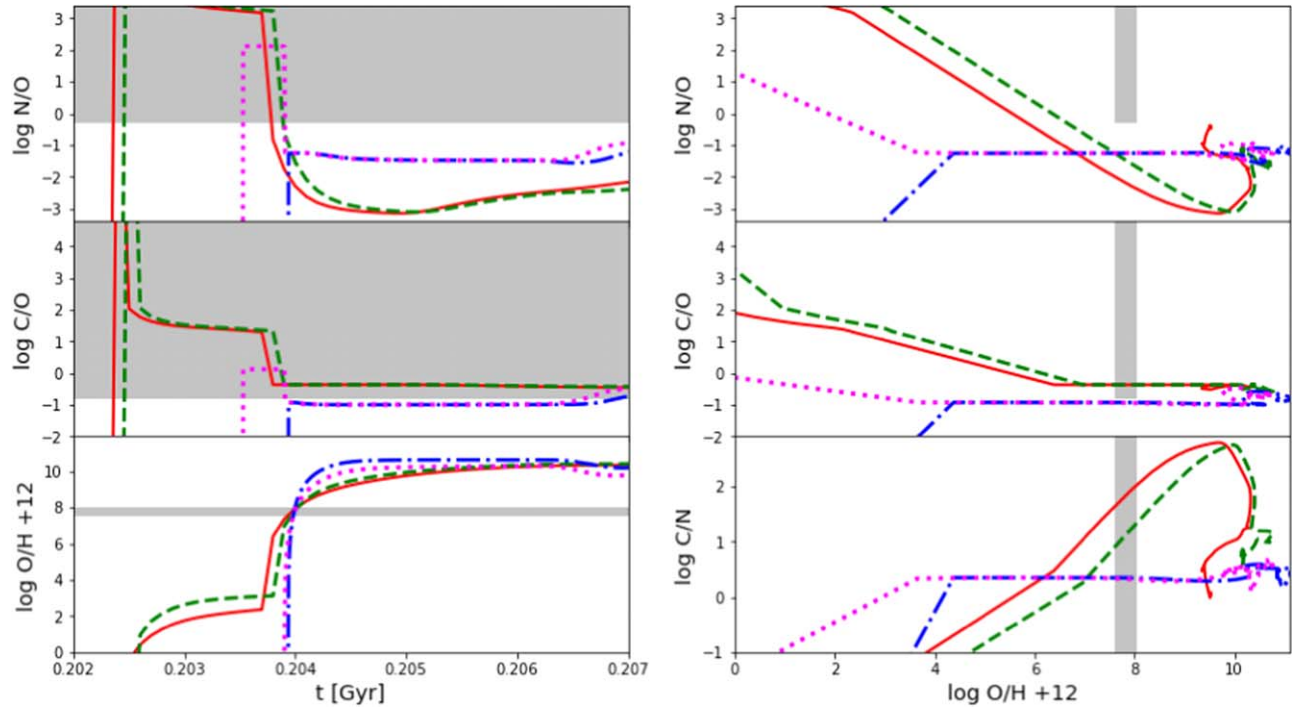

Figure 3. Evolution of CNO abundance ratios (by number) vs. time (left) and gas oxygen abundance (right) for single starburst models with different IMFs. The standard model includes WR stars assuming Kroupa IMF with massive-end slope of $x = 1.3$ (red solid lines). The additional curves assume instead a top-heavy IMF for Population III stars with a slope $x = 0$ in the mass range 30–120$M_\odot$ (green short dashed), 100–280$M_\odot$ to add PISNe (blue long dashed), and 100–1000$M_\odot$ to add VMSs (magenta dotted). Gray areas/bars are the observational data for GN-z11 (Cameron et al. 2023).

general relativistic instability before igniting H-burning (Fuller et al. 1986). Incomplete core H burning has been proposed as an explanation for the abundance anomaly (Denissenkov & Hartwick 2014), and the so-called O–Na anticorrelation (Kraft et al. 1997) often seen in globular clusters of the Milky Way. These stars have been invoked also to account for the high N/O ratio measured in GN-z11 (Nagele & Umeda 2023), although lower-mass stars survive until He-burning and enhance C and O. However, the structure and evolution depend not only on their initial masses and metallicities, but also their formation path (Woods et al. 2019). In a very narrow mass range, zero-metallicity stars may explode as general relativistic supernovae (Chen et al. 2014), which will have a significant effect and would be inconsistent with the observation of GN-z11.

4.2. CNO Evolution

The IMF dependence on the CNO tracks are shown in Figure 3 as a function of time (left) and ISM oxygen abundance (right). In order to maximize the impact of VMSs, a top-heavy IMF is assumed for Population III stars with a flat mass distribution ($x = 0$). At low metallicities, compared to the standard IMF (red solid lines), a top-heavy[11] Population III IMF up to $m_u = 120M_\odot$ (green short dashed) can produce up to ~1 dex systematic increase of N/O. If the Population III IMF is extended up to $m_u = 280M_\odot$ (blue long dashed), PISNe produce a large amount of Fe and also O, and the initial (C,N)/O ratios become very low. Finally, if the Population III IMF is extended up to $m_u = 1000M_\odot$ (magenta dotted), the initial (C,N)/O ratios can become high again due to the VMS contribution (Section 4.1).

[11] We adopt $m_\ell = 30M_\odot$ for Population III to minimize O production from core-collapse supernovae.

In the last two models with $m_u > 120M_\odot$, while PISNe are assumed to occur only from Population III stars, VMSs produce some metals via winds also at higher metallicities. This causes a ~2 dex increase of N at intermediate metallicities (log O/H +12 ~ 8), which is, however, insufficient to match the observed range of GN-z11. Larger m_u values do not increase the N/O ratio further because of the Population I/II IMF slope of $x = 1.3$. The VMS contribution is washed out once AGB stars start producing N at high metallicities. Also note that VMSs decrease C (as it is transformed into N), and these two models do not reproduce the observed C/O ratio either.

5. Conclusions

We have presented, for the first time, a chemical evolution model that naturally explains the "anomalous" elemental abundance ratios of GN-z11. Without changing the IMF or the nucleosynthesis yields, the observed data can be reproduced if this galaxy has experienced a star formation history featuring a quiescent phase, lasting ~100 Myr, separating two strong starbursts. Importantly, the observed ratios cannot be explained by single burst models with VMSs and/or PISNe. Essentially, this is because VMSs do not increase N/O sufficiently, while PISNe rather decrease N/O ratios.

In our successful models, prior to the observed epoch ($z = 10.6$), the galaxy has been chemically enriched. This pre-enrichment is likely caused by internal, rather than external, sources. For a brief period after the second burst, WR stars (up to 120$M_\odot$) become the dominant enrichment source, which explains the high (C,N)/O ratios at the observed metallicity of GN-z11. WR stars also enhance particular elements (N, F, Na, and Al; see the Appendix) and isotopes (^{13}C and ^{18}O); the prediction of high fluorine abundance can be tested with ALMA (e.g., Franco et al. 2021).

Our results strongly suggest that super-early galaxies undergo a feedback-regulated, stochastic (Pallottini & Ferrara 2023), or even intermittent (Cole et al. 2023), star formation history. In spite of this, detecting the chemical anomalies (e.g., high N/O) produced by multiple bursts might not be easy as the chemical evolution proceeds quite rapidly, thus erasing this signature on short timescales ($\lesssim$1 Myr). This scenario is also consistent with the presence of strong radiation-driven outflows (Carniani et al. 2023), which are necessary to clear the dust produced by the observed stars in super-early galaxies like GN-z11 (Ferrara et al. 2023; Fiore et al. 2023; Ziparo et al. 2023). At lower redshifts ($z \sim 7$), dust instead may accumulate inside galaxies, which might correspond to dusty galaxies observed by ALMA (e.g., Dayal et al. 2022).

Our findings highlight the potential of chemical evolution models and data on elemental abundances (and isotopic ratios), not only to investigate the physics and evolution of the most distant galaxies but also to provide new constraints on nuclear and stellar astrophysics.

Acknowledgments

We acknowledge the stimulating atmosphere of the IFPU Focus Week (2023 May), where this work has been initially worked out. We thank M. Limongi, K. Takahashi, and G. Volpato for providing the nucleosynthesis data. C.K. acknowledges funding from the UK Science and Technology Facility Council through grant ST/R000905/1, ST/V000632/1. The work was also funded by a Leverhulme Trust Research Project Grant on "Birth of Elements." Support from ERC Advanced Grant INTERSTELLAR H2020/740120 (A.F.) is kindly acknowledged.

DATA AVAILABILITY

The data underlying this article will be shared on reasonable request to the corresponding author.

Appendix

Our conclusions are based on the following parameter study. The left panels of Figure 4 show a variety of dual burst models that can reproduce the observations, compared to the fiducial model (red solid line); the differences are small depending on the details of the dual burst models. (i) If the duration of the first burst and/or interval between the two bursts are short ($t_1 = 0.05$, $t_2 = 0.1$ Gyr; green short dashed), similar CNO tracks are obtained, with a slightly lower peak N/O ratio. (ii) If no interval ($t_1 = t_2 = 0.1$ Gyr; blue long dashed) is assumed, the peak N/O ratio is only marginally consistent with data, since the metallicity decrease due to dilution after the secondary gas inflow is weaker. (iii) Similar CNO tracks are also obtained with longer inflow timescales ($\tau_i = 0.01$ Gyr), which also result in a higher star formation rate at the observed

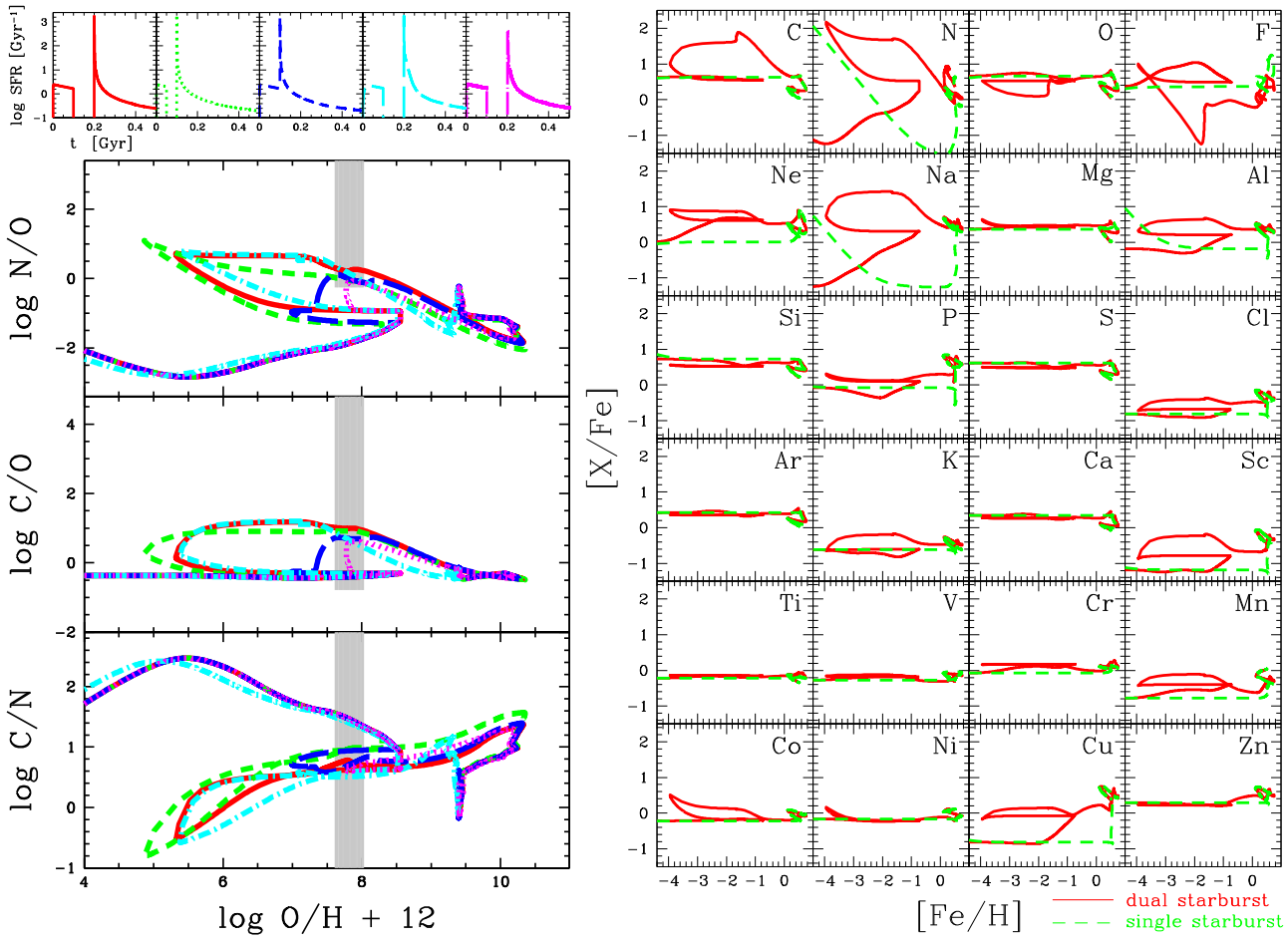

Figure 4. Left: same as the middle panel of Figure 2 but for a variety of dual burst models assuming a shorter interval (green short dashed line), no interval (blue long dashed), longer τ_i (cyan dotted–dashed), and shorter $\tau_{s,2}$ (magenta dotted), compared to the fiducial model (red solid). The corresponding star formation histories are shown on the top panels. Right: the [X/Fe]–[Fe/H] relations for the dual (red solid line) and single (green dashed) burst models in Figure 2.

epoch. (iv) Finally, with a weaker second burst ($\tau_{s,2} = 0.001$ Gyr), the N/O ratio becomes lower, and the condition to reach the observed N/O is $\tau_{s,2} \leqslant 1$ Myr.

Our GCE models can predict elemental abundances and isotopic ratios, self-consistently. The right panels of Figure 4 show the [X/Fe]–[Fe/H] relations of all stable elements from C to Zn, for our fiducial, dual burst model (red solid line) and a single burst model (green dashed). For GN-z11, it would be difficult to measure the abundances of elements other than CNO. Nevertheless, these predictions can be compared with peculiar stars in the Milky Way to study its formation process.

ORCID iDs

Chiaki Kobayashi https://orcid.org/0000-0002-4343-0487
Andrea Ferrara https://orcid.org/0000-0002-9400-7312

References

Abel, T., Bryan, G. L., & Norman, M. L. 2002, Sci, 295, 93
Aguado, D. S., Salvadori, S., Skúladóttir, Á., et al. 2023, MNRAS, 520, 866
Barkat, Z., Rakavy, G., & Sack, N. 1967, PhRvL, 18, 379
Beers, T. C., & Christlieb, N. 2005, ARA&A, 43, 531
Bekki, K., & Tsujimoto, T. 2023, MNRAS: Letters, 526, L26
Bromm, V., & Larson, R. B. 2004, ARA&A, 42, 79
Bunker, A. J., Saxena, A., Cameron, A. J., et al. 2023, A&A, 677, A88
Burrows, A., & Vartanyan, D. 2021, Natur, 589, 29
Cameron, A. J., Katz, H., Rey, M. P., & Saxena, A. 2023, MNRAS, 523, 3516
Carniani, S., Venturi, G., Parlanti, E., et al. 2023, arXiv:2306.11801
Cayrel, R., Depagne, E., Spite, M., et al. 2004, A&A, 416, 1117
Charbonnel, C., Schaerer, D., Prantzos, N., et al. 2023, A&A, 673, L7
Chen, K. J., Heger, A., Woosley, S., et al. 2014, ApJ, 790, 162
Cole, J. W., Papovich, C., Finkelstein, S. L., et al. 2023, arXiv:2312.10152
Dayal, P., Ferrara, A., Sommovigo, L., et al. 2022, MNRAS, 512, 989
Denissenkov, P. A., & Hartwick, F. D. A. 2014, MNRAS, 437, L21
Ferrara, A., Pallottini, A., & Dayal, P. 2023, MNRAS, 522, 3986
Ferrara, A., Sommovigo, L., Dayal, P., et al. 2022, MNRAS, 512, 58
Fiore, F., Ferrara, A., Bischetti, M., Feruglio, C., & Travascio, A. 2023, ApJL, 943, L27
Franco, M., Coppin, K. E. K., Geach, J. E., et al. 2021, NatAs, 5, 1240
Fuller, G. M., Woosley, S. E., & Weaver, T. A. 1986, ApJ, 307, 675
Gelli, V., Salvadori, S., Ferrara, A., Pallottini, A., & Carniani, S. 2023, ApJL, 954, 11
Greif, T. H., Springel, V., White, S. D. M., et al. 2011, ApJ, 737, 75
Hartwig, T., Ishigaki, M. N., Kobayashi, C., Tominaga, N., & Nomoto, K. 2023, ApJ, 946, 20
Heger, A., & Woosley, S. E. 2002, ApJ, 567, 532
Higgins, E. R., Vink, J. S., Hirschi, R., Laird, A. M., & Sabhahit, G. N. 2023, MNRAS, 526, 543
Hirano, S., Hosokawa, T., Yoshida, N., et al. 2014, ApJ, 781, 60
Inami, H., Algera, H., Schouws, S., et al. 2022, MNRAS, 515, 100
Ishigaki, M. N., Tominaga, N., Kobayashi, C., & Nomoto, K. 2018, ApJ, 857, 46
Isobe, Y., Ouchi, M., Tominaga, N., et al. 2023, ApJ, 959, 100
Janka, H. T. 2012, ARNPS, 62, 407
Kobayashi, C., Karakas, A. I., & Lugaro, M. 2020a, ApJ, 900, 179
Kobayashi, C., Leung, S. C., & Nomoto, K. 2020b, ApJ, 895, 138
Kobayashi, C., & Nakasato, N. 2011, ApJ, 729, 16
Kobayashi, C., & Nomoto, K. 2009, ApJ, 707, 1466
Kobayashi, C., & Taylor, P. 2023, in Handbook of Nuclear Physics, ed. Tanihata, Toki, & Kajino (Singapore: Springer),
Kobayashi, C., Tominaga, N., & Nomoto, K. 2011, ApJL, 730, L14
Kobayashi, C., Tsujimoto, T., & Nomoto, K. 2000, ApJ, 539, 26
Kraft, R. P., Sneden, C., Smith, G. H., et al. 1997, AJ, 113, 279
Kroupa, P. 2008, in ASP Conf. Ser. 390, Pathways Through an Eclectic Universe, ed. J. H. Knapen, T. J. Mahoney, & A. Vazdekis (San Francisco, CA: ASP), 3
Lau, R. M., Hankins, M. J., Han, Y., et al. 2022, NatAs, 6, 1308
Limongi, M., & Chieffi, A. 2018, ApJS, 237, 13
Looser, T. J., D'Eugenio, F., Maiolino, R., et al. 2023, arXiv:2302.14155
Marques-Chaves, R., Schaerer, D., Kuruvanthodi, A., et al. 2024, A&A, 681, A30
Martinet, S., Meynet, G., Nandal, D., et al. 2022, A&A, 664, A181
Meynet, G., & Maeder, A. 2002, A&A, 390, 561
Nagele, C., & Umeda, H. 2023, ApJL, 949, L16
Nomoto, K., Kobayashi, C., & Tominaga, N. 2013, ARA&A, 51, 457
Pallottini, A., & Ferrara, A. 2023, A&A, 677, L4
Rossi, M., Salvadori, S., & Skúladóttir, Á 2021, MNRAS, 503, 6026
Saccardi, A., Salvadori, S., D'Odorico, V., et al. 2023, ApJ, 948, 35
Schneider, F. R. N., Sana, H., Evans, C. J., et al. 2018, Sci, 359, 69
Senchyna, P., Plat, A., Stark, D. P., & Rudie, G. C. 2023, arXiv:2303.04179
Skúladóttir, Á., Salvadori, S., Amarsi, A. M., et al. 2021, ApJL, 915, L30
Smartt, S. J. 2009, ARA&A, 47, 63
Stacy, A., & Bromm, V. 2013, MNRAS, 433, 1094
Szécsi, D., Agrawal, P., Wünsch, R., & Langer, N. 2022, A&A, 658, A125
Takahashi, K., Yoshida, T., & Umeda, H. 2018, ApJ, 857, 111
Todini, P., & Ferrara, A. 2001, MNRAS, 325, 726
Umeda, H., & Nomoto, K. 2003, Natur, 422, 871
Vink, J. S., Muijres, L. E., Anthonisse, B., et al. 2011, A&A, 531, A132
Volpato, G., Marigo, P., Costa, G., et al. 2023, ApJ, 944, 40
Witstok, J., Shivaei, I., Smit, R., et al. 2023, Natur, 621, 267
Woods, T. E., Agarwal, B., Bromm, V., et al. 2019, PASA, 36, e027
Yusof, N., Hirschi, R., Meynet, G., et al. 2013, MNRAS, 433, 1114
Ziparo, F., Ferrara, A., Sommovigo, L., & Kohandel, M. 2023, MNRAS, 520, 2445